LAWRENCE
LIVERMORE
NATIONAL
LABORATORY

UCRL-JRNL-215368

In-Situ Phase Mapping and Direct Observations of Phase Transformations During Arc Welding of 1045 Steel

J. Elmer, T. Palmer

September 14, 2005

Metallurgical and Materials Transactions A

Disclaimer

In-Situ Phase Mapping and Direct Observations of Phase Transformations During Arc Welding of 1045 Steel

by
J. W. Elmer and T. A. Palmer
Lawrence Livermore National Laboratory, Livermore, CA

Abstract

In-situ Spatially Resolved X-Ray Diffraction (SRXRD) experiments were performed during gas tungsten arc (GTA) welding of AISI 1045 C-Mn steel. Ferrite (α) and austenite (γ) phases were identified and quantified in the weld heat-affected zone (HAZ) from the real time x-ray diffraction data. The results were compiled along with weld temperatures calculated using a coupled thermal fluids weld model to create a phase map of the HAZ. This map shows the $\alpha \rightarrow \gamma$ transformation taking place during weld heating and the reverse $\gamma \rightarrow \alpha$ transformation taking place during weld cooling. Superheating is required to complete the $\alpha \rightarrow \gamma$ phase transformation, and the amount of superheat above the A3 temperature was shown to vary with distance from the centerline of the weld. Superheat values as high as 250°C above the A3 temperature were observed at heating rates of 80°C/s. The SRXRD experiments also revealed details about the γ phase not observable by conventional techniques, showing that γ is present with two distinct lattice parameters as a result of inhomogeneous distribution of carbon and manganese in the starting pearlitic/ferritic microstructure. During cooling, the reverse $\gamma \rightarrow \alpha$ phase transformation was shown to depend on the HAZ location. In the fine grained region of the HAZ, at distances greater than 2 mm from the fusion line, the $\gamma \rightarrow \alpha$ transformation begins near the A3 temperature and ends near the A1 temperature. In this region of the HAZ where the cooling rates are below 40°C/s, the transformation occurs by nucleation and growth of pearlite. For HAZ locations closer to the fusion line, undercoolings of 200°C or more below the A1 temperature are required to complete the $\gamma \rightarrow \alpha$ transformation. In this region of the HAZ, grain growth coupled with cooling rates in excess of 50°C/s causes the transformation to occur by a bainitic mechanism.

Introduction

The optimized base metal properties of steels are altered during welding due to the severe thermal cycles that result from by the localized welding heat source. As a result, non-equilibrium microstructures are created in the fusion zone (FZ) and heat affected zone (HAZ) of the weld that differ significantly in appearance and properties from those found in the base metal [1-3]. Transformations between the body centered cubic (bcc) ferritic form of iron and the face centered cubic (fcc) austenitic form of iron are principally responsible for the changes in microstructure. It is well known that carbon plays an important role in these transformations [1-3], and that increasing the carbon content will increase both degree of microstructural changes that occur and the amount of non-equilibrium phases that are created during welding. In order to better understand the microstructural evolution in steel welds, in-situ x-ray diffraction studies are being performed to directly observe the phase transformations that occur during welding of low and medium carbon steels.

Time Resolved X-Ray Diffraction (TRXRD) has recently been used to investigate phase transformations that occurred during stationary GTA spot welding of both medium carbon (AISI 1045) [4] and low carbon (AISI 1005) steels [5]. These real-time synchrotron-based experiments tracked phase transformations in the heat-affected zone of welds under rapid heating and cooling rates in excess of 100°C/s. The results were used to quantify the relative fractions of α and γ phases during weld heating and cooling with 100 ms time resolution. Modeling of the TRXRD spot welds was performed using a transient 3-D coupled thermal fluids code to determine the time-temperature profile of the welds [6]. Differences in austenitization rates of the low and high carbon steels were observed, and were attributed to differences in amounts and distributions of the pearlite and allotriomorphic ferrite phases in the base metal microstructures [4].

Spatially Resolved X-Ray Diffraction (SRXRD) has also been used to investigate phase transformations in the low carbon steel [7-12]. From these results, a map of the phases present in the HAZ was created for this steel that showed the locations of the γ and α phases during welding [7, 8]. Kinetic modeling of the $\alpha \rightarrow \gamma$ phase transformation data from the SRXRD experiments was performed using a Johnson-Mehl-Avrami (JMA) approach in order to determine JMA kinetic parameters for the 1005 steel under real welding conditions [9-12]. Using this kinetic description of the $\alpha \rightarrow \gamma$ phase transformation and other phase transformation models, time temperature transformation (TTT) and continuous heating transformation (CHT)

diagrams were constructed and were used to predict microstructure evolution [8]. In the medium carbon steel, the influence of weld heat input on the width of the $\alpha+\gamma$, and γ phase regions in the HAZ was determined using the SRXRD technique [13, 14]. These experiments revealed an additional observation, whereby the γ phase in the 1045 steel was observed to exist with two distinct lattice parameters which caused a distinct splitting of the γ x-ray diffraction peaks at temperatures just above the A3 temperature. The split peaks eventually combined into one diffraction peak as diffusion of C and Mn homogenized the microstructure at HAZ temperatures near the solidus temperature of the alloy.

In this investigation, the medium carbon steel containing 0.46 wt% C was further investigated using the SRXRD technique in order to create a complete map of the phases that exist in the HAZ during welding. This map is similar to the map previously created for the low carbon steel weld [7, 8], and provides a means to compare the kinetics of the $\alpha \rightarrow \gamma$ phase transformation in steels with two different carbon contents (0.05 and 0.46 wt%C). Quantitative information about the phase transformation kinetics was extracted from this data through thermal and phase transformation modeling. The results presented here demonstrate the differences in the phase transformation behavior between low and medium carbon steels, and show how in situ x-ray diffraction can be used to provide real time observations of important phase transformations during the welding of steels.

Experimental Procedures

SRXRD Experiments

Gas tungsten arc (GTA) welds were made on AISI 1045 steel cylindrical forged bar samples (0.46 C, 0.85 Mn, 0.27 Si, 0.02 Ni, 0.11 Cr, 0.014 P, 0.01 Cu, 0.02 S, 0.027 Al, 0.001 Nb, 0.01 Mo, 0.005 V; by wt. percent). These samples were machined from 10.8 cm diameter forged bar stock into welding samples, 12.7 cm long and 10.2 cm diameter. Welds were then made on the cylindrical steel bars in an environmentally sealed chamber to avoid atmospheric contamination of the weld. A schematic illustration of the experimental setup is shown in Fig. 1, and a brief summary of the welding parameters is given in Table 1. Additional details of similar welding experiments are reported elsewhere [7, 8, 14].

The *in-situ* SRXRD experiments were performed during welding using the 31-pole wiggler beam line, BL 10-2 at SSRL with SPEAR (Stanford Positron-Electron Accumulation

Ring) operating at an electron energy of 3.0 GeV and an injection current of approximately 100 mA. Fig. 1 illustrates the SRXRD setup where a focused monochromatic synchrotron x-ray beam is passed through a 260 μm tungsten pinhole to render a sub-millimeter beam on the sample at an incident angle of ~25°. This arrangement yields a beam flux on the sample of ~10^{11} photons/s, which was measured experimentally using an ion chamber immediately downstream from the pinhole. A photon energy of 12.0 keV (λ = 0.1033 nm) was chosen for these experiments, since this energy is far enough above the Fe K-edge (7.112 keV) to minimize the background contribution due to Fe K-fluorescence from the steel sample. The background radiation was further reduced using a thin Nb foil (25 μm), which was placed directly in front of the detector to act as a filter.

X-ray diffraction patterns were recorded using a 50 mm long 2048 element position sensitive Si photodiode array detector. The array was mounted on a dual-stage water cooled Peltier effect thermoelectric cooler at a distance of approximately 10 cm behind the weld to cover a 2θ range from 22° to 52°. This 2θ range was optimized to contain a total of six diffraction peaks, three from the α phase and three from the γ phase, as indicated in the calculated x-ray diffraction pattern for iron in Fig. 2. Calibration of the x-ray diffraction patterns was performed using a thin niobium foil that has a well characterized bcc crystal structure. This foil was placed directly on the bar to be welded, allowing an initial diffraction pattern to be taken of it just prior to initiating the weld.

Diffractions patterns were taken during welding by incrementing the weld with respect to the x-ray beam in 0.2 mm steps perpendicular to the welding direction. Post-weld analysis of each peak in every diffraction pattern was performed to determine the semi-quantitative volume fractions of γ and α present as a function of welding time. This analysis measured the integrated intensity of each peak using a sum of one or more Gaussian peak profile fitting functions using an automated curve-fitting routine developed in Igor Pro®, Version 4.0 [15]. The raw integrated intensities of the diffraction peaks were then converted into phase fractions as described in more detail elsewhere [8].

Phase Equilibria and Base Metal Microstructure

The phase transformation sequence of the 1045 steel was calculated from thermodynamic relationships using Thermocalc, version 2 for Windows, and the TCFE2 database [16]. These

calculations were used to determine the transformation temperatures for the AISI 1045 steel by considering the effects of Fe, C, Si, Mn, Ni and Cr on the liquid, ferrite, austenite, and cementite phase fields. The calculated phase transformation temperatures for this multi-component alloy are illustrated in the pseudo-binary diagram shown in Fig. 3, where the vertical dashed line indicates the nominal carbon content of the alloy.

The thermodynamic calculations indicate that the equilibrium starting microstructure of this alloy will consist of a mixture of α and Fe_3C carbide phases. During heating this microstructure will begin to transform to γ at a calculated A1 temperature of 712ºC, while complete transformation will occur at a calculated A3 temperature of 765ºC. The γ that forms will remain stable until melting begins to occur at a calculated solidus temperature of 1410ºC. Note that δ ferrite does not form in this alloy since the δ ferrite field exists only for lower carbon contents than 0.45% in this steel. The transformations that occur during heating reverse during cooling, however, kinetic limitations may alter the predicted phase transformation start and completion temperatures, and may produce non-equilibrium phases.

The starting microstructure of the 1045 steel is shown in Fig. 4a as revealed by polishing the base meal and etching in a 2% nital (nitric acid and alcohol) solution. This microstructure contains allotriomorphic ferrite, which is the light etching phase that outlines the prior γ grain boundaries. Inside the prior γ grains, the microstructure consists of pearlitie colonies that etch dark and occupy the majority of the microstructure. A higher magnification micrograph highlighting the lamellar structure of the pearlite is shown in Fig. 4b. Quantitative metallography was performed on this microstructure using Image Pro®, Ver. 4.1. Measurements of the area fraction of allotriomorphic ferrite made at several locations indicate that the microstructure contains 12% allotriomorphic ferrite, and 88% pearlite. The prior γ grain size of the base metal was measured to be 92.8 μm in diameter. In addition, the size of the allotriomorphic grain boundary α phase was shown to be 15 μm to 20 μm wide, with some patches reaching 30 μm or more in places.

Coupled Thermal-Fluids Numerical Modeling of Weld Temperatures

The SRXRD experimental results provide information about phase transformations as a function of location around the weld, but do not directly provide information about weld temperatures. In order to relate weld location to weld temperature, a numerical model was used

since transient weld temperatures are difficult to measure accurately. The weld model employed here is a well tested 3D numerical heat transfer and fluid flow model, which is described in more detail in references [17, 18] and has been applied to similar SRXRD welding experiments as discussed elsewhere [10, 11].

The thermal calculations are made under steady-state conditions in a fixed Cartesian coordinate system attached to and moving with the heat source. Since the weld pool displays a mirror symmetry, calculations are performed on only half the workpiece, and a flat weld pool surface is assumed. The electromagnetic, surface tension gradient, and buoyancy driving forces present in the transient weld pool convection are taken into account during these calculations. A computational domain of 76×43×44 grid points encompassing a volume having dimensions of 410 mm long, 20 mm wide, and 23 mm deep was used. Non-uniform grid spacing, with finer grids located near the heat source where the temperature gradients were the highest, was also utilized for maximum resolution of the variables. The boundary conditions used in these calculations are similar to those used in previous studies [13, 14]. The thermo-physical properties used to represent the 1045 steel alloy in these calculations are given in Table 2 [19, 20].

The calculated weld pool dimensions and selected isotherms were then compared with the experimental weld pool dimensions and also to the first appearance of γ in the SRXRD results. The cross sectional shape of the calculated weld pool at its maximum size matched the experimental weld cross section having a width just under 10 mm and a depth of 5.7 mm In addition, the weld model was used to calculate thermal profiles in the HAZ at different distances from the weld centerline. Figure 5 shows the calculated temperature profiles in 1 mm increments across the width of the HAZ. These temperatures are also compared with the phase transformation temperatures predicted from thermodynamics (see Fig. 3), and will be used later to calculate heating and cooling rates in the HAZ as well as the peak temperatures experienced in different portions of the HAZ.

The important isotherms for the 1045 steel are the A1 (712ºC) where the microstructure begins to transform to γ on heating, the A3 (765ºC) where complete transformation to γ will occur on heating, and the melting point of 1410ºC. During cooling these same isotherms are important, plus two additional ones representing the bainite start (485ºC) and the martensite start temperatures (324ºC) [4].

In addition to calculating the temperature distribution around the weld, the model was

used to calculate the temperature profiles and the heating/cooling rates at specific HAZ locations. Figure 5 showed the results of these calculations where the temperature profiles were taken at different distances parallel to the welding direction, showing how the distance from the weld centerline influences the peak temperatures and overall thermal cycles of the weld. The HAZ can be approximated as the region between the melting point of the steel at the Y=5.0 mm location, and the A1 temperature which has its peak near the Y=10 mm location. Within this region, the range of heating rates at the A1 temperature for this weld were calculated to vary from approximately 80ºC/s near the fusion line to 25ºC/s near the edge of the HAZ, whereas the cooling rates are smaller and vary from 60ºC/s near the fusion line to 10ºC/s near the edge of the HAZ.

Results

SRXRD Semi-Quantitative Phase Map

The SRXRD experimental data were first used to identify the spatial distribution of the α, and γ phases in the weld HAZ. Each diffraction pattern was further analyzed to determine the amount of α and γ at each discreet location in the HAZ using a structure factor approach that is summarized in reference [8]. The final results are given in Table 3, which shows the relative fraction of γ for the front (heating) side of the weld for each of the SRXRD runs. In this table, the fraction γ is given at each SRXRD location starting close to the weld centerline (Y=0) and moving out through the HAZ to a position in the base metal at approximately Y=10 mm. Twelve different SRXRD runs are indicated for the heating side of the weld, starting at a location far enough ahead of the weld where no transformation was observed (X= -9 mm), and moving back to the position where the transformation to austenite was furthest from the centerline of the weld (X=2 mm). Since the temperatures are highest near the centerline of the weld, the formation of austenite at these locations is either complete or nearly so. At further distances from the weld centerline, α begins to co-exist with γ in increasing proportions. An α/γ co-existence region is found in a band around the weld that is 1-1.6 mm wide, and only α is observed outside of this α/γ co-existence band.

Table 4 summarizes the relative γ fractions for the back (cooling) side of the weld. In this table, the γ fraction is again given at each SRXRD location starting close to the weld centerline (Y=0) and moving out through the HAZ to a position Y=10 mm. Thirteen additional

SRXRD paths are indicated, starting at the X=3 mm position and moving back to the X=15 mm position. The region of co-existence between γ and α returns towards the centerline of the weld as the α→γ phase transformation occurs during cooling. Additional SRXRD data was taken out to the X=24 mm location, however, this region of the weld contained primarily α in the HAZ and is not shown in this Table. Data from the resolidified portion of the weld (Y<5.0 mm) is not reliable due to surface roughness that interferes with the x-ray beam and is not reported here.

A phase map of the weld HAZ was developed from the SRXRD measurements that plots the γ fraction in the regions undergoing the α→γ and γ→α phase transformations during welding. This map is shown in Fig. 6 with calculated weld isotherms superimposed over the SRXRD data. In the plot, the shading indicates the γ fraction, which varies from 0% γ (blue) to 100% γ (red). The individual SRXRD line scans were made perpendicular to the welding direction, and show a variation in γ from 0 to 100% over a narrow region approximately 1.0 to 1.6 mm wide. These regions indicate where the α→γ phase transformation is taking place in the weld HAZ.

The map shown in Fig. 6 plots the locations of the α and γ phases with 0.2 mm precision perpendicular to the welding direction, and 0.5 mm parallel to the welding direction. It is clear that a large γ phase field surrounds the weld pool, and that this phase field is expanded on the trailing side of the weld as compared to the A3 isotherm at 765°C. No δ ferrite was observed at the fusion line, which is consistent with the phase diagram shown in Fig. 3. It is apparent from the location of the γ phase field with respect to the A3 isotherm, that the completion of the α→γ phase transformation is shifted to higher temperatures on heating and to lower temperatures on cooling relative to the A3 isotherm. It is also apparent that the γ phase field on the trailing side of the weld has a shape dissimilar to that of the A3 isotherm whereby the γ region extends much further behind the isotherm in the region close to the fusion line (5<Y<7 mm) than it does further out from the fusion line.

The isotherms superimposed on the SRXRD data in Fig. 6 were calculated from the coupled thermal fluids weld model discussed earlier in this paper. Differences between the measured and calculated location of the γ phase field is evidence of the non-equilibrium conditions that exist during welding. The results indicate that some degree of superheat is required to completely transform the microstructure to γ on heating, and some degree of

undercooling is required to initiate the transformation to α on cooling. In general, the lag required to complete the transformation to γ on heating follows the A3 isotherm, but is displaced further from the A3 isotherm at locations closer to the weld centerline where the heating rates are the highest. This suggests that the amount of superheating required for the α→γ transformation varies with heating rate. The behavior on the cooling side of the weld is a bit different whereby the region closest to the fusion zone requires considerable undercooling prior to measurable amounts of transformation to α being measured as compared to locations further from the fusion line that transforms close to the A3 isotherm.

Discussion

The α→γ phase transformation on heating

In the experiments performed here, the α→γ transformation was experimentally measured using the SRXRD technique for weld heating rates that were calculated to vary between 25 and 80ºC/s. This data can be compared to the α→γ transformation rates for the same steel at higher heating rates of the TRXRD experiments [4] and also for the low carbon 1005 steel under similar heating conditions observed using SRXRD [7, 8].

The regions of the weld that are most useful to understand the microstructural evolution are the regions where both the α and γ phases coexist, since this is where the α→γ phase transformation is taking place. The coexistence region was observed in the SRXRD scans to occur between X=-6 mm and X=2 mm, and each of these nine data sets are plotted in Fig 7. This plot shows the individual SRXRD data points as a function of distance from the weld centerline where coexistence of α and γ was observed, and a best fit line is drawn through each set. The SRXRD data were fit using a 4-parameter sigmoidal relationship of the form:

$$\gamma = \gamma_o + a(1+\exp(-(y-y_o)/b))^{-1} \qquad \text{Eq. (1)}$$

In this expression γ_o, a, y_o and b are the parameters being fit, while γ represents the measured fraction of γ at the Y distance away from the centerline of the weld. The two parameters that control the position and shape of the transformation curve are y_o and 'b', while 'a' and γ_o represent the base line γ values of approximately 0 and 100% respectively. The y_o parameter

gives the y-axis distance from the centerline of the weld where the transformation is 50% complete, while b represents the rate at which the transformation takes place. Table 5 further summarizes the fit parameters y_o and b for the heating side of the weld.

During heating, the $\alpha \rightarrow \gamma$ transformation curves move outward to larger Y-values because of the increasing temperature, which is indicated by the increasing value of y_o. The rate of the $\alpha \rightarrow \gamma$ transformation represented by the b parameter has a value -0.157+0.029, and does not change significantly with location. The relatively constant value of the b parameter indicates that the $\alpha \rightarrow \gamma$ transformation is taking place at essentially the same rate over the entire leading edge of the weld HAZ.

The phase map shown in Fig. 6 can also be used to determine the amount of superheat above the A3 temperature required to completely transform the microstructure to γ. Comparisons between the location of the fully transformed γ phase field and the A3 isotherm show that the superheat varies with location, apparently due to the effect of heating rate which increases as the weld centerline is approached. At locations close to the weld centerline the amount of superheat is on the order of 250°C, whereas further out (X>7 mm) the amount of superheat is approximately 50°C or less. The results from the 1005 steel were also similar, where the average superheat above the A3 temperature was measured to be 135°C, with a maximum value of approximately 250°C close to the centerline of the weld [8].

The $\gamma \rightarrow \alpha$ phase transformation on cooling

The transformations that occur during cooling of the steel can be more complicated than those observed during heating because of the potential for the formation of non-equilibrium phases, especially at high cooling rates. It is already known that diffusion dependant transformations, such as the formation of pearlite which has a lamellar microstructure of alternating ferrite and cementite phases, occur at low cooling rates [3]. As the cooling rate increases, diffusion of carbon may not be rapid enough to allow the lamellar pearlite microstructure to form. Shear-type transformations begin to take place at these higher cooling rates and lead to the formation of non-equilibrium phases. Bainite is one constituent that can form at higher cooling rates, and is characterized by a microstructure of mixed ferrite and cementite with non-lamellar features. Bainite forms through a combination of diffusion and shear at intermediate cooling rates, at temperatures above the martensite start temperature [3].

Martensite is the other non-equilibrium constituent that forms in steels at high rates, and does so entirely by a shear mechanism. The martensitic microstructure contains lath or plate-like characteristics with the carbon trapped in interstitial sites of the crystal lattice [3].

The formation of bainite and martensite cannot be described by the equilibrium phase diagram presented in Fig. 3 since these transformations occur under nonequilibrium conditions. However, one can use calculated continuous cooling transformation (CCT) diagrams to provide information about microstructural evolution during weld cooling. In a previous study [4], the model developed by Bhadeshia et al [21, 22] was used to predict the continuous cooling transformation diagram for the AISI 1045 steel. The results showed that a cooling rate faster than 10ºC/s is required to initiate bainite formation. Moreover, a cooling rate in excess of 60ºC/s is required to initiate the formation of martensite. The bainite start temperature for this 1045 steel was calculated to be 485ºC, and the martensite start temperature was calculated to be 324ºC. Both of these temperatures are far below the equilibrium A1 temperature, thus requiring significant undercooling prior to the formation of bainite or martensite.

In the TRXRD experiments performed in the previous study on 1045 steel [4] the cooling rates were well in excess of 100ºC/s and therefore produced a predominantly martensitic microstructure. In the SRXRD welding experiments in this investigation, the cooling rates were lower, and would not be expected to produce a significant amount of martensite. The thermal profiles shown in Fig. 5 were analyzed to calculate the heating and cooling rates in the HAZ near at the A1 temperature. These results showed that near the fusion line (Y=5 mm), the heating and cooling rates peaked at approximately 80 and 60ºC/s respectively. Further out in the HAZ (Y=10 mm) the heating rate at the A1 temperature was approximately 25ºC/s, while the cooling rate was approximately 15ºC/s. Therefore, the formation of bainite is likely to occur in the HAZ of these welds, but only in the region of the HAZ closest to the fusion line where the cooling rates are the highest. Pearlite would be expected to form further out from the centerline of the weld where the cooling rates are lower.

Thus the possibility exists that the HAZ is formed by two different mechanisms during cooling in this weld as a result of the variation in cooling rates in the HAZ. The likelihood of two different $\gamma \rightarrow \alpha$ transformation mechanisms is confirmed by the SRXRD results shown in Fig. 6. This figure shows that the $\gamma \rightarrow \alpha$ transformation deviates significantly from the curvature of the A3 isotherms for HAZ locations between the fusion line and Y=7 mm, where the indicated

transformation temperature is significantly below the A3, and that the $\gamma \rightarrow \alpha$ transformation begins at a temperature close to the bainite start of 485ºC.

Optical metallography was performed on the as welded sample to compare the microstructures formed in the two different regions of the HAZ. Fig. 8a shows the microstructure near the HAZ/base metal boundary (Y=8 mm) that was fully austenitized during heating. This post weld microstructure consists of fine grains having an average diameter of approximately 20μm, which is smaller than those of the base metal microstructure. The fine grained microstructure of this portion of the HAZ is largely pearlitic with a small lamellar spacing. The fine grains form as a result of numerous nucleation sites within the original pearlitic microstructure (see Fig 4), coupled with insufficient time for grain growth to occur. During cooling, the relatively low cooling rates and small γ grain size allowed the $\gamma \rightarrow \alpha$ transformation to occur through the reformation of pearlite.

Fig. 8b shows the HAZ near the fusion line, which has a significantly different microstructure than that shown in Fig. 8a. In this microstructure, the prior γ grains are visible and are lightly outlined by allotriomorphic ferrite. The grain size here is significantly larger than that of the base metal, having an average diameter greater than 100 μm, which results from the high peak temperatures which approach the melting point of the alloy in this region of the HAZ. The transformed microstructure in this region of the HAZ is characteristic of bainite, having a lath type appearance forming along multiple crystallographic variants.

The calculated weld isotherms superimposed on the SRXRD data in Fig 6 provide further evidence for the formation of bainite adjacent to the fusion line. This bainite start temperature isotherm coincides with the $\gamma \rightarrow \alpha$ transformation along the trailing side of the weld. Thus, the SRXRD data mapping of the HAZ confirms the transformation of γ into both pearlitic and bainitic regions, and indicates where these transformations take place relative to the fusion line of the weld.

Splitting of Austenite Peaks

Previous in-situ SRXRD x-ray observations have shown that the γ phase can exist with two different lattice parameters in this steel during weld heating [13, 14]. The two different lattice parameters resulted in a measurable splitting of the SRXRD austenite diffraction peaks. The splitting was attributed to the presence of two types of austenite: a low carbon austenite,

which is believed to form from allotriomorphic ferrite; and a high carbon austenite, which is believed to form from the pearlitic regions of the starting microstructure. During welding, these two types of austenite appeared at different stages of the weld thermal cycles but eventually combined into one diffraction peak with one lattice parameter as the C and Mn diffused and redistributed into one homogeneous austenite phase at high temperatures. The inhomogeneous formation of austenite was observed under both high [13], and low [14] heating rate conditions in the 1045 steel.

Analysis of the diffraction peaks in the data from this study also indicate split austenite peaks in the weld HAZ. Figure 9a shows an fcc(111) diffraction pattern from a region of the weld close to the fusion line where only a single austenite peak was observed (X=0, Y=5.0), while Fig. 9b shows a diffraction pattern along this same path from a region of the HAZ further from the centerline where peak splitting was observed (X=0, Y=5.8). It is apparent that the austenite is forming with two different lattice parameters in these experiments as well. This type of splitting was observed in all of the x-ray scans that passed through the completely austenitized region of the HAZ in this study.

The results of the analysis of the peak split regions of the x-ray diffraction patterns are summarized in Fig. 10. In this plot the start and end points of the peak split region are indicated for each of the SRXRD scans through the HAZ. The triangular symbols indicate the boundary where the split peak is first observed, and the square symbols indicate the boundary where the peaks completely merge at higher temperatures. During weld heating, the peak splitting is first observed at locations very close to the point when the microstructure has been completely transformed to austenite at temperatures above the A3 temperature. This plot indicates that the first occurrence of peak splitting occurs at similar temperatures within the HAZ, since the trend of the data roughly parallels the isotherms on the heating side of the weld. The location of the HAZ where the split peaks combine to form a single peak during heating occurs at temperatures around 1400°C, which is near the solidus temperature of this steel. During weld cooling, the peak split region is observed to continue to be present until the austenite back transforms to ferrite behind the weld.

Comparison of 1045 and 1005 HAZ Transformation Kinetics

The results from the previous SRXRD study that mapped the γ and α phase fields of the steel containing 0.05wt% carbon [4] can be compared to the results from this study on 0.45wt%

carbon steel. The phase map for the low carbon steel weld showed that the $\alpha \rightarrow \gamma$ transformation on the heating side of the weld is similar to that of the medium carbon steel. In each case, the $\alpha \rightarrow \gamma$ transformation follows the A1 temperatures on the heating side of the weld and complete transformation to γ is not observed until the temperatures exceed the A3. In both steels, the average superheating required to complete the $\alpha \rightarrow \gamma$ transformation follows similar trends, whereby the superheat increases with increasing heating rate closer to the centerline of the weld. Also in both steels, the $\alpha+\gamma$ region was shown to exist in a band approximately 1-1.5 mm wide that roughly parallels the A1 and A3 isotherms up to the point where the cooling transformation begins.

Using the semi-quantitative data for the $\alpha \rightarrow \gamma$ phase transformation for the 1005 steel [8], each SRXRD data trace was also fit to the sigmoidal relationship of eq. 1. The fitting parameters y_o and b, were then determined and are plotted in Fig. 11 along with those of the 1045 steel of this investigation. It is clear from this figure that the transformation rate, which is related to 'b', is similar for both steels and does not change significantly with weld location. The average values of this parameter are $b=-0.157 \pm 0.029$ for the 1045 steel, and $b=-0.175 \pm 0.061$ for the 1005 steel, where the standard deviation is indicated. The slightly more negative value for the 1005 steel indicates that this transformation is taking place faster and over a slightly more narrow range than for the 1045 steel. The larger difference in Fig. 11 is the comparison between the y_o values for the two different steels, which are related to the distance from the centerline of the weld where the transformation takes place. The larger y_o values for the 1045 steel indicate that the $\alpha \rightarrow \gamma$ transformation is taking place further out from the centerline of the weld than for 1005 steel. One reason for this is that the welding parameters used in the two SRXRD studies were not identical, whereby those used in the 1045 steel welds were approximately 20% higher in power than those used in the 1005 steel welds. The different heat inputs were required from the different fluid flow characteristics of each steel. The 1045 steel, with higher sulfur content, required a higher heat input than the 1005 steel to produce the same weld pool width.

Even with the different heat inputs, the two steels display similar transformation characteristics during heating. For example, both show a band of $\alpha+\gamma$ coexistence of approximately 1-1.5 mm wide that roughly parallels the A1 and A3 isotherms, but is displaced behind these isotherms indicating that superheating is required to initiate and complete the $\alpha \rightarrow \gamma$ transformation. The location of the 50 % transformation line, indicated by y_o, lies just above the

A3 isotherm for both steels and the transformation rate, as indicated by 'b', indicates that the range where both phases coexist is slightly larger for the higher sulfur content 1045 steel.

During weld cooling the 1005 and 1045 steels behave differently. In the 1005 steel [8], the $\gamma \rightarrow \alpha$ transformation parallels the A1 isotherm, wrapping around the back side of the weld. Throughout the entire HAZ this transformation was largely complete when the A1 temperature was reached, which would be expected for transformation via a nucleation and growth mechanism. In contrast, the 1045 steel displays two different transformation mechanisms on cooling. For the fine grained region of the HAZ farther from the weld fusion line, the transformation is similar to that of the 1005 steel, where the transformation is largely complete when the A1 temperature is reached. However for regions closer to the fusion line, in the large grained region of the HAZ, the $\gamma \rightarrow \alpha$ transformation of the 1045 steel required significantly higher undercoolings to complete the transformation. These large undercoolings are associated with the formation of bainite, that begins to form from γ at 485°C, and was confirmed through post weld optical metallographic characterization.

Conclusions

1. In situ SRXRD experiments were used to map the phases present in the HAZ during GTA welding of AISI 1045 steel, while a 3D coupled thermal fluids model was used to calculate both the shape of the liquid weld pool and the temperature distribution in the HAZ. The resulting map plots the phases present around the HAZ during welding with sub-millimeter precision, and compares the phase fields with the phase transformation isotherms. The results show a relatively large austenite field surrounding the weld pool, and the evolution of this phase field during weld heating and cooling.
2. A comparison of the SRXRD measured location of the single phase austenite region with the calculated A3 temperatures for this steel shows that the amount of superheat required to complete the $\alpha \rightarrow \gamma$ phase transformation during weld heating increases with heating rate. Superheating as high as 250 above the A3 temperature was observed in the region of the HAZ with the highest heating rate of 80°C/s.
3. During weld heating, γ was observed to exist with two different lattice constants which resulted in a splitting of the γ diffraction peaks. The peak splitting appears to be caused

by the formation of low carbon and high carbon constituents due to the inhomogeneous starting microstructure that consists of low C/Mn allotriomorphic ferrite, and high C/Mn pearlite. These two different austenite phases homogenize to form one austenite peak in the high temperature regions of the HAZ that are located close to the weld fusion line.

4. Two different $\gamma \rightarrow \alpha$ phase transformation behaviors were observed during weld cooling. In the fine grained region of the HAZ at distances greater than approximately 2 mm from the fusion line, the transformation completed at temperatures close to the A1 temperature with only small amounts of undercooling. For distances within 2 mm of the fusion line, the $\gamma \rightarrow \alpha$ transformation occurred with undercoolings on the order of 200°C below the A1 temperature. This difference in transformation behavior corresponds to nucleation and growth of pearlite at locations far from the fusion line, and the formation of bainite closer to the fusion line where the grains are larger and the cooling rates are higher.
5. The kinetics of the $\alpha \rightarrow \gamma$ transformation in the 1045 steel were compared to those of the 1005 steel that was previously mapped using the SRXRD technique [8]. During heating, both steels behaved similarly, requiring similar superheating above the A3 temperature to complete the $\alpha \rightarrow \gamma$ transformation. During cooling, the 1005 steel completed the $\gamma \rightarrow \alpha$ transformation near its A1 temperature for all regions of the HAZ. However, the 1045 steel showed a deviation from this trend close to the fusion line where the bainitic transformation was observed at temperatures significantly lower than the A1 temperature.

Acknowledgments

This work was performed under the auspices of the U. S. Department of Energy by UC, Lawrence Livermore National Laboratory, under Contract No. W-7405-ENG-48. Portions of this work were supported by DOE, Office of Basic Energy Sciences, Division of Materials Science. The synchrotron aspects of this research were carried out at the Stanford Synchrotron Radiation Laboratory, a national user facility operated by Stanford University on behalf of the U.S. Department of Energy, Office of Basic Energy Sciences. The authors would like to express their gratitude to Mr. Bob Vallier of LLNL for performing the metallographic characterization of the base metal and welded samples.

References

1. Ø. Grong: Metallurgical Modelling of Welding, *The Institute of Materials*, London, Chapter 1, 1994.

2. M. F. Ashby and K. E. Easterling, "A First Report on Diagrams for Grain Growth in Welds," *Acta Metall*., V30, p. 1969, 1982.

3. J. C. Ion, K. E. Easterling, and M. F. Ashby, "A Second Report on Diagrams of Microstructure and Hardness for Heat-Affected Zones in Welds," *Acta Metall*., V32, p. 1949, 1984.

4. J. W. Elmer, T. A. Palmer, S. S. Babu, W. Zhang and T. Debroy, "Direct Observations of Austenite, Bainite, and Martensite Formation During Arc Welding of 1045 Steel using Time Resolved X-ray Diffraction," *Welding Journal*, V83(9), pp 244-s to 253-s, September, 2004.

5. Joe Wong, T. Ressler and J. W. Elmer, "Dynamics of Phase Transformations and Microstructure Evolution in Carbon-Manganese Steel Arc Welds Using Time Resolved Synchrotron X-Ray Diffraction," *J. Synchrotron Radiation*, 10: pp. 154-167 Part 2 Mar 2003.

6. W. Zhang, G. G. Roy, J. W. Elmer, and T. DebRoy, "Modeling of Heat Transfer and Fluid Flow during GTA Spot Welding of 1005 Steel," *Journal of Applied Physics*, V93(5), pp. 3022-3033, 1 Mar., 2003.

7. J. W. Elmer, Joe Wong and Thorsten Ressler, "Spatially Resolved X-Ray Diffraction Mapping of Phase Transformations in the HAZ of Carbon-Manganese Steel Arc Welds," *Metall. and Mater. Trans. A*, 32A (5), pp. 1175-1187, 2001.

8. J. W. Elmer, T. A. Palmer, W. Zhang, B. Wood, and T. DebRoy, "Kinetic Modeling of Phase Transformations Occurring in the HAZ of C-Mn Steel Welds Based on Direct Observations," *Acta Materialia*, V51, pp. 3333-3349, 2003.

9. W. Zhang, J. W. Elmer, and T. Debroy, "Integrated modeling of thermal cycles, austenite formation, grain growth and decomposition in the heat affected zone of carbon steel," *Science and Technology of Welding and Joining*, V10(5), pp 574-582, 2005.

10. W. Zhang, J. W. Elmer, and T. DebRoy, "Kinetics of Ferrite to Austenite Phase Transformation during Welding of 1005 Steel," *Scripta Materialia*, 46, pp753-757, 2002.

11. W. Zhang, J. W. Elmer, and T. DebRoy, "Modeling and Real Time Mapping of Phases during GTA Welding of 1005 Steel," *Materials Science and Engineering A*, vol. 333 (1-2), pp. 320-335, 2002.

12. A. Kumar, S. Mishra, J. W. Elmer and T. DebRoy, "Optimization of Johnson Mehl Avrami Equation Parameters for α-Ferrite to γ-Austenite Transformations in Steel Welds using a Genetic Algorithm," *Metallurgical and Materials Transactions A*, 36A (1), pp. 15-

22, January 2005.

13. T. A. Palmer and J. W. Elmer, "Direct Observations of the Nucleation and Growth of Austenite from Pearlite and Allotriomorphic Ferrite in a C-Mn Steel Arc Weld," *Scripta Materialia*, V53(5), pp 535-540, 2005.

14. T. A. Palmer and J. W. Elmer, "Effects of Input Power on the α–γ Phase Transformation in the HAZ of 1045 C-Mn Steel Arc Welds Observed by Spatially Resolved X-Ray Diffraction," in press, *Metallurgical and Materials Transactions A*, March, 2005.

15. S. Babu, Private communications, Oak Ridge National Laboratory, 2002.

16. B. Sundman, B. Jansson and J. Andersson, *Calphad-Computer Coupling of Phase Diagrams and Thermochemistry*, V 9(2), p.153, 1985.

17. K. Mundra, T. DebRoy, and K. Kelkar, *Numerical Heat Transfer*, (29), pp. 115-129, 1996.

18. Z. Yang and T. DebRoy: *Metall. Mater. Trans. B*, 1999, vol. 30B, pp. 483-493.

19. M.W. Chase, Jr., C.A. Davies, J.R. Downey, Jr., D.J. Frurip, R.A. Mcdonald, and A.N. Syverud: *JANAF Thermochemical Tables*, 3rd Edition, American Chemical Society and American institute for Physics, Washington, DC, 1985.

20. E.A. Brandes, ed.: *Smithells Metals Reference Book*, 7th Edition, London: Butterworth and Heinemann, 1992.

21. HKDH Bhadesia, L. E. Svensson., B. Gretoft, "A Model for the Development of Microstructure in Low-Alloy Steel (FE-MN-SI-C) Weld Deposits," *Acta Metallurgica*, 33 (7), p. 1271, 1985.

22. HKDH Bhadesia, "Thermodynamic Analysis of Isothermal Transformation Diagrams," *Metal Science*, 16 (3), p. 159, 1982.

Tables

Table 1: Summary of GTA welding parameters used in the SRXRD experiments.

Welding Electrode	W-2% Th
Electrode Diameter (mm)	4.7
Torch Polarity	DCEN
Maximum Current (A)	175
Background Current (A)	123
Pulsing Frequency (Hz)	300
Peak On Time (%)	50
Arc Voltage (V)	16.2
Weld Speed (mm/s)	0.6
Shielding Gas	Helium
Resulting Fusion Zone Width (mm)	10.0
Resulting Fusion Zone Depth (mm)	5.6

Table 2. Summary of material and modeling parameters used in heat transfer modeling of weld pool size and shape.

Material Parameters	
Density of Liquid (gm/cm^3)	7.87
Effective Viscosity of Liquid (gm/cm-sec)	0.75
Solidus Temperature (K)	1694
Liquidus Temperature (K)	1767
Enthalpy of Solid at Melting Point (cal/gm)	251
Enthalpy of Liquid at Melting Point (cal/gm)	315.5
Specific Heat of Solid (cal/gm-K)	0.095
Specific Heat of Liquid (cal/gm-K)	0.3
Thermal Conductivity of Solid (cal/cm-sec-K)	0.1
Effective Thermal Conductivity of Liquid (cal/cm-sec-K)	0.215
Coefficient of Thermal Expansion (1/K)	$1.0x10^{-5}$
d(gamma)/dT of pure material (dynes/cm-K)	-0.155
Concentration of Surface Active Species (wt%)	0.020
Surface Excess at Saturation ($mole/cm^2$)	$1.3x10^{-9}$
Enthalpy of Segregation (cal/mole)	$-3.97x10^{4}$
Entropy Factor	$3.2x10^{-3}$
Weld Parameters	
Arc Efficiency	0.85
Arc Radius (mm)	0.295
Preheat Temperature (^oC)	200

Table 3: Semi-quantitative analysis showing the austenite fraction at each of the SRXRD locations on the heating side of the weld (X<3 mm).

	X=-9.0	-8.0	-7.0	-6.0	-5.0	-4.0	-3.0	-2.0	-1.0	0.0	1.0	2.0
Y=0	0.0	0.0	4.1	100.0	100.0							
0.2	0.0	0.0	17.2	100.0	100.0							
0.4	0.0	0.0	34.6	100.0	100.0							
0.6	0.0	0.0	28.4	100.0	100.0							
0.8	0.0	0.0	29.7	100.0	100.0							
1.0	0.0	0.0	20.7	100.0	100.0							
1.2	0.0	0.0	24.0	100.0	100.0							
1.4	0.0	0.0	23.8	100.0	100.0							
1.6	0.0	0.0	15.0	100.0	100.0							
1.8	0.0	0.0	14.3	100.0	100.0							
2.0	0.0	0.0	6.7	100.0	100.0							
2.2	0.0	0.0	7.9	92.1	100.0							
2.4	0.0	0.0	0.0	96.7	100.0							
2.6	0.0	0.0	0.0	95.7	100.0	100.0						
2.8	0.0	0.0	0.0	89.9	100.0	100.0						
3.0	0.0	0.0	0.0	93.0	100.0	100.0						
3.2	0.0	0.0	0.0	79.3	100.0	100.0						
3.4	0.0	0.0	0.0	67.1	100.0	100.0	100.0					
3.6	0.0	0.0	0.0	37.0	100.0	100.0	100.0					
3.8	0.0	0.0	0.0	11.1	100.0	100.0	100.0					
4.0	0.0	0.0	0.0	2.1	100.0	100.0	100.0					
4.2	0.0	0.0	0.0	0.6	100.0	100.0	100.0					
4.4	0.0	0.0	0.0	10.4	100.0	100.0	100.0					
4.6	0.0	0.0	0.0	7.2	100.0	100.0	100.0	100.0				
4.8	0.0	0.0	0.0	0.0	94.3	100.0	100.0	100.0				
5.0	0.0	0.0	0.0	0.0	83.0	100.0	100.0	100.0				
5.2	0.0	0.0	0.0	0.0	64.8	100.0	100.0	100.0		100.0	100.0	100.0
5.4	0.0	0.0	0.0	0.0	64.3	100.0	100.0	100.0	100.0	100.0	100.0	100.0
5.6	0.0	0.0	0.0	0.0	37.6	100.0	100.0	100.0	100.0	100.0	100.0	100.0
5.8	0.0	0.0	0.0	0.0	2.0	100.0	100.0	100.0	100.0	100.0	100.0	100.0
6.0	0.0	0.0	0.0	0.0	5.3	96.1	100.0	100.0	100.0	100.0	100.0	100.0
6.2	0.0	0.0	0.0	0.0	3.9	89.5	100.0	100.0	100.0	100.0	100.0	100.0
6.4	0.0	0.0	0.0	0.0	3.9	57.5	100.0	100.0	100.0	100.0	100.0	100.0
6.6	0.0	0.0	0.0	0.0	0.0	31.4	100.0	100.0	100.0	100.0	100.0	100.0
6.8	0.0	0.0	0.0	0.0	0.0	6.6	100.0	100.0	100.0	100.0	100.0	100.0
7.0	0.0	0.0	0.0	0.0	0.0	0.0	100.0	100.0	100.0	100.0	100.0	100.0
7.2	0.0	0.0	0.0	0.0	0.0	0.0	100.0	100.0	100.0	100.0	100.0	100.0
7.4	0.0	0.0	0.0	0.0	0.0	0.0	100.0	100.0	100.0	100.0	100.0	100.0
7.6	0.0	0.0	0.0	0.0	0.0	0.0	100.0	100.0	100.0	100.0	100.0	100.0
7.8	0.0	0.0	0.0	0.0	0.0	0.0	98.1	100.0	100.0	100.0	100.0	100.0
8.0	0.0	0.0	0.0	0.0	0.0	0.0	90.2	98.2	100.0	100.0	100.0	100.0
8.2	0.0	0.0	0.0	0.0	0.0	0.0	83.8	88.1	100.0	100.0	100.0	100.0
8.4	0.0	0.0	0.0	0.0	0.0	0.0	73.9	58.9	99.8	100.0	100.0	100.0
8.6	0.0	0.0	0.0	0.0	0.0	0.0	33.3	21.6	97.8	99.0	100.0	100.0
8.8	0.0	0.0	0.0	0.0	0.0	0.0	17.8	6.6	88.0	91.4	100.0	100.0
9.0	0.0	0.0	0.0	0.0	0.0	0.0	7.3	0.6	48.3	92.8	91.1	99.8
9.2	0.0	0.0	0.0	0.0	0.0	0.0	2.9	1.2	21.0	68.4	92.0	99.8
9.4	0.0	0.0	0.0	0.0	0.0	0.0	0.0	0.0	6.9	50.4	90.0	88.9
9.6	0.0	0.0	0.0	0.0	0.0	0.0	0.0	0.0	0.0	18.3	71.3	63.8
9.8	0.0	0.0	0.0	0.0	0.0	0.0	0.0	0.0	0.0	2.9	34.6	29.3
10.0	0.0	0.0	0.0	0.0	0.0	0.0	0.0	0.0	0.0	0.0	19.1	4.8
10.2	0.0	0.0	0.0	0.0	0.0	0.0	0.0	0.0	0.0	0.0	7.1	0.0
10.4	0.0	0.0	0.0	0.0	0.0	0.0	0.0	0.0	0.0	0.0		

Table 4: Semi-quantitative analysis showing the austenite fraction at each of the SRXRD locations on the cooling side of the weld for 3<X<15mm.

	X=3.0	4.0	5.0	6.0	7.0	8.0	9.0	10.0	11.0	12.0	13.0	14.0	15.0
Y=0.0													
0.2													
0.4													
0.6													
0.8													
1.0													
1.2													
1.4													
1.6													
1.8													
2.0													
2.2													
2.4													
2.6													
2.8													
3.0													
3.2													
3.4													
3.6													
3.8													
4.0													
4.2													
4.4													
4.6													
4.8													
5.0	100	100.0	100.0	100.0	100.0	100.0	100.0	100.0	100.0	100.0	100.0	100.0	39.6
5.2	100	100.0	100.0	100.0	100.0	100.0	100.0	100.0	100.0	100.0	100.0	100.0	6.2
5.4	100	100.0	100.0	100.0	100.0	100.0	100.0	100.0	100.0	100.0	100.0	39.8	10.0
5.6	100	100.0	100.0	100.0	100.0	100.0	100.0	100.0	100.0	100.0	100.0	99.7	69.6	2.4
5.8	100	100.0	100.0	100.0	100.0	100.0	100.0	100.0	100.0	100.0	100.0	86.2	31.1	1.0
6.0	100	100.0	100.0	100.0	100.0	100.0	100.0	100.0	100.0	99.8	76.3	5.2	0.2
6.2	100	100.0	100.0	100.0	100.0	100.0	100.0	100.0	100.0	96.5	52.1	2.4	0.0
6.4	100	100.0	100.0	100.0	100.0	100.0	100.0	100.0	100.0	80.7	27.9	0.5	0.0
6.6	100	100.0	100.0	100.0	100.0	100.0	100.0	100.0	100.0	62.6	12.1	0.1	0.0
6.8	100	100.0	100.0	100.0	100.0	100.0	100.0	100.0	100.0	26.3	0.0	0.0	0.0
7.0	100	100.0	100.0	100.0	100.0	100.0	100.0	100.0	100.0	17.2	0.0	0.0	0.0
7.2	100	100.0	100.0	100.0	100.0	100.0	100.0	100.0	96.3	2.4	0.0	0.0	0.0
7.4	100	100.0	100.0	100.0	99.9	100.0	99.8	100.0	97.3	0.1	0.0	0.0	0.0
7.6	100	100.0	100.0	100.0	89.2	100.0	99.2	99.3	90.3	0.0	0.0	0.0	0.0
7.8	100	100.0	100.0	100.0	89.5	99.9	92.8	72.7	80.2	0.0	0.0	0.0	0.0
8.0	100	100.0	100.0	100.0	59.2	89.1	68.8	74.2	64.1	0.0	0.0	0.0	0.0
8.2	100	99.8	95.1	100.0	27.7	75.5	36.1	39.4	39.5	0.0	0.0	0.0	0.0
8.4	99.9	92.5	94.0	100.0	12.8	51.9	18.5	33.3	18.0	0.0	0.0	0.0	0.0
8.6	88.7	77.7	80.5	93.8	0.7	34.6	6.0	22.8	1.2	0.0	0.0	0.0	0.0
8.8	61.1	45.4	47.9	74.8	0.0	17.4	0.9	19.4	0.0	0.0	0.0	0.0	0.0
9.0	27.3	12.4	34.6	53.3	0.0	9.1	0.0	8.5	0.0	0.0	0.0	0.0	0.0
9.2	6.6	6.2	33.7	19.6	0.0	0.0	0.0	0.0	0.0	0.0	0.0	0.0	0.0
9.4	0.0	0.2	0.5	1.1	0.0	0.0	0.0	0.0	0.0	0.0	0.0	0.0	0.0
9.6		0.2	0.0	0.0	0.0	0.0	0.0	0.0	0.0	0.0	0.0	0.0	0.0
9.8		0.0	0.0	0.0	0.0	0.0	0.0	0.0	0.0	0.0	0.0	0.0	0.0

Table 5: Summary of the sigmoidal fit parameters for the $\alpha \rightarrow \gamma$ phase transformation on heating. The parameter 'y0' is the location where 50% of the transformation has been completed, and the parameter 'b' is related to the rate of the transformation. Results from the 1045 steel from this study are compared to those from a previous investigation of 1005 steel [8].

X	1045 Steel		1005 Steel	
(mm)	y_o	b	y_o	b
-6	3.51	-0.162		
-5	5.43	-0.220		
-4	6.36	-0.173	2.72	-0.305
-3	6.92	-0.164	4.24	-0.221
-2	7.84	-0.123	5.08	-0.105
-1	8.18	-0.173	5.59	-0.147
0	8.41	-0.126	6.03	-0.154
1	8.37	- 0.156	6.40	-0.128
2	8.48	-0.132	6.66	-0.144
3	8.66	-0.135	7.09	-0.122

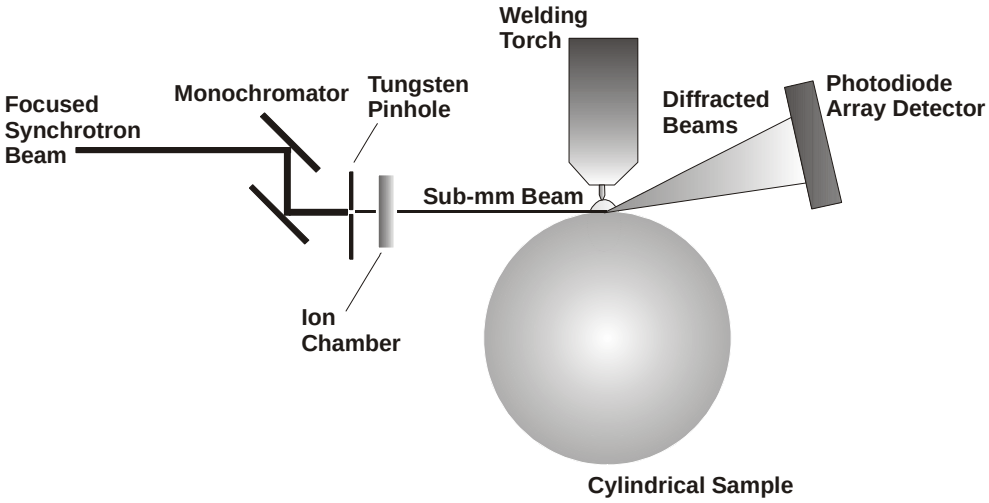

Figure 1: Schematic diagram of the SRXRD experimental setup for synchrotron based in-situ observations of phase transformations during welding.

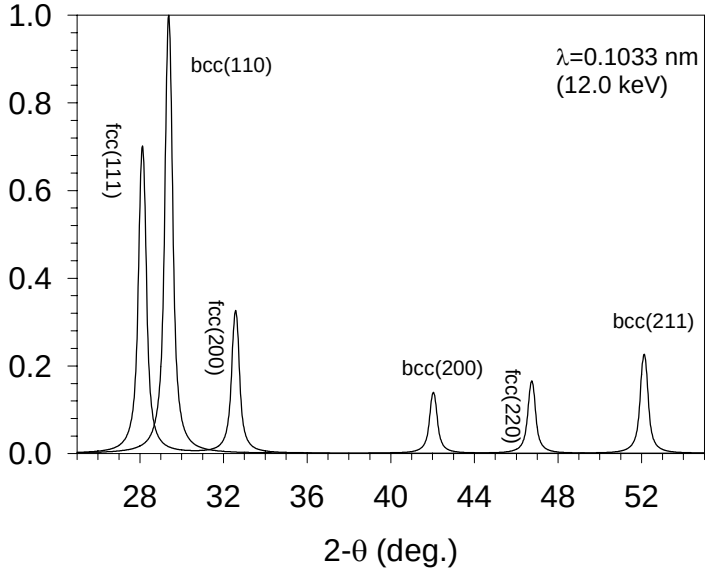

Figure 2: Calculated diffraction pattern of iron, showing the 3 possible peaks for each phase that can appear in the detector window. Equal amounts of the fcc and bcc phases are assumed.

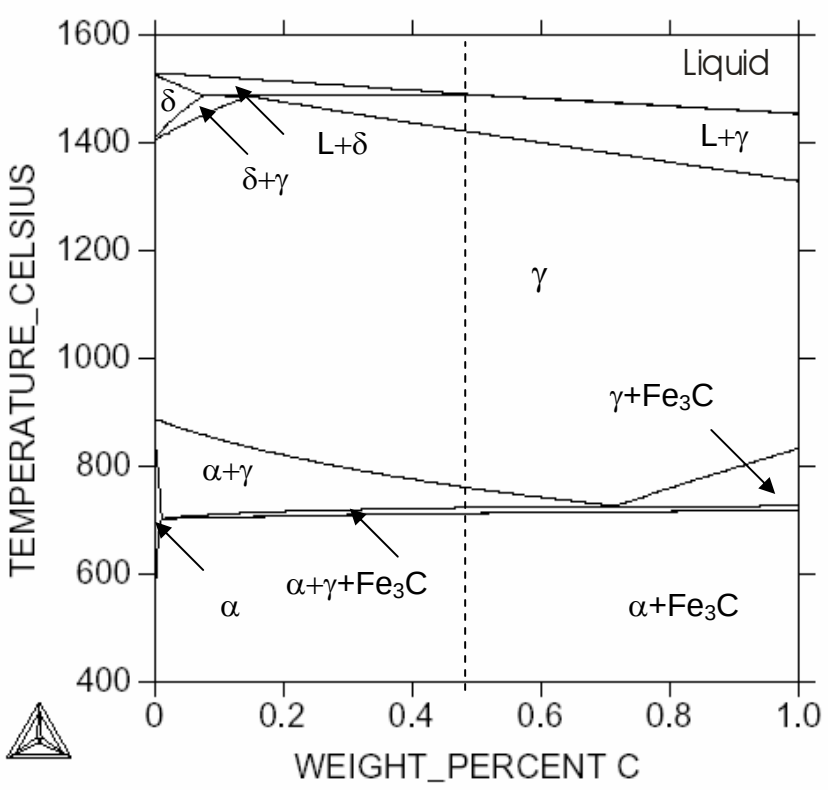

Figure 3: Calculated pseudobinary phase diagram for the AISI 1045 steel. The nominal carbon concentration of the alloy is indicated as the vertical dashed line.

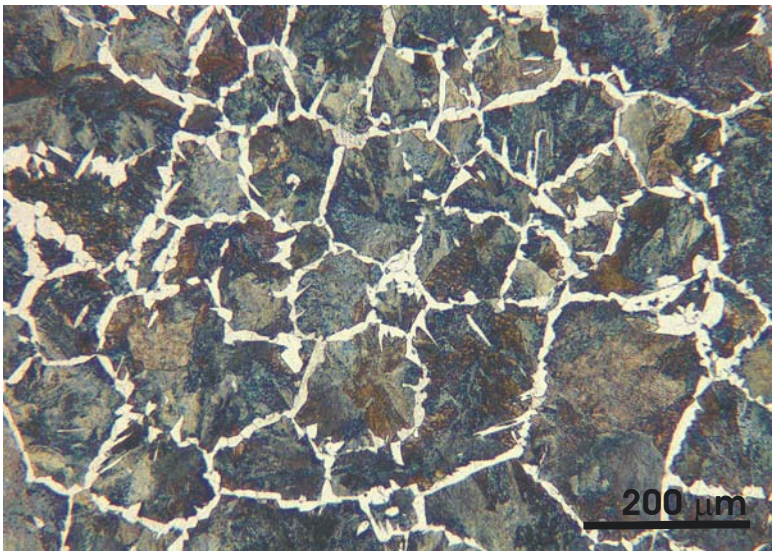

Figure 4a: Base metal microstructure showing allotrimorphic ferrite outlining the prior austenite grains and pearlite colonies inside the grains.

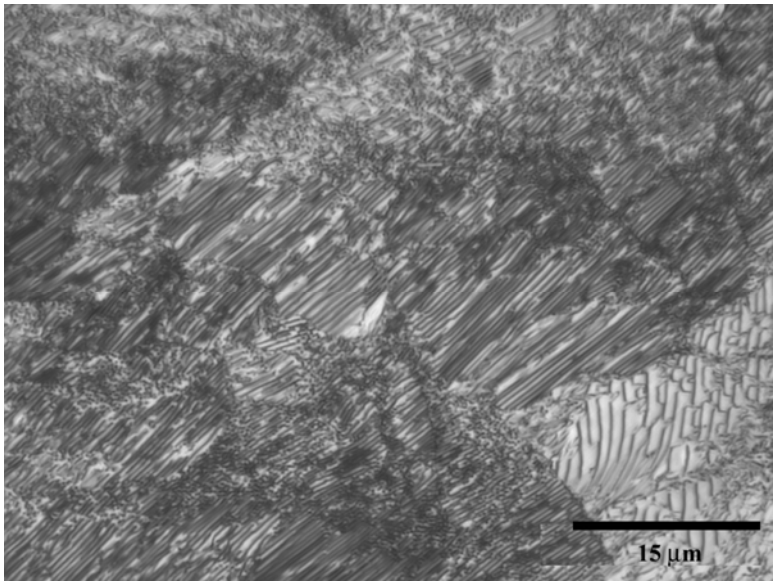

Figure 4b. High magnification optical micrograph showing the lamellar microstructure typical of the pearlite colonies within the grains.

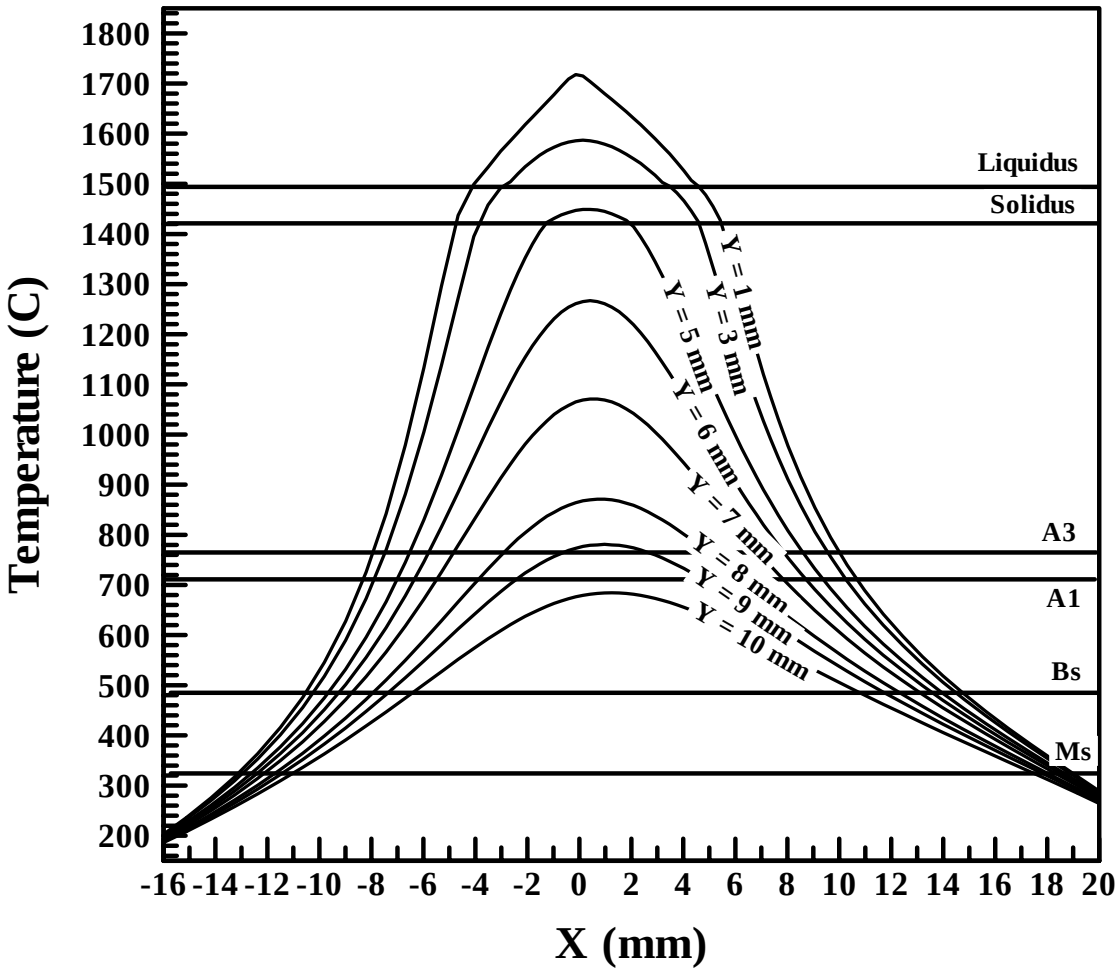

Figure 5: Calculated heating and cooling rates through the HAZ for different distances from the centerline of the weld. Phase transformation temperatures are indicated by the horizontal lines.

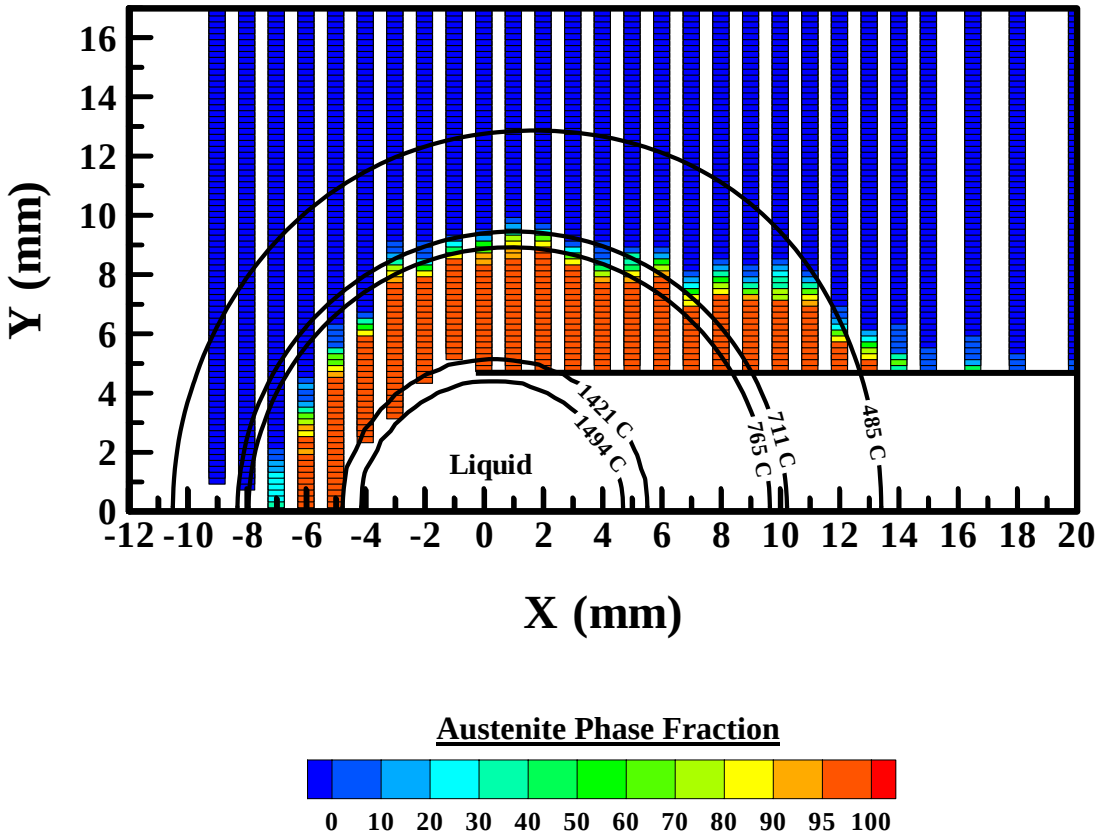

Figure 6: SRXRD map showing the amount of austenite and ferrite in existing in the HAZ of 1045 steel, overlaid with the calculated weld isotherms.

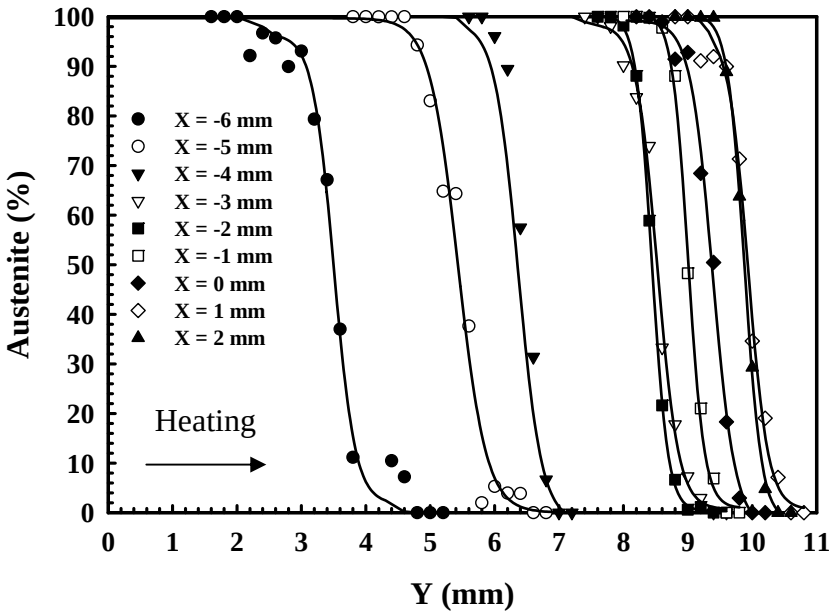

Figure 7: SRXRD measured austenite fractions plotted versus weld position for the $\alpha \rightarrow \gamma$ transformation on the heating side of the weld (data points), and the best fit sigmoidal curves (lines).

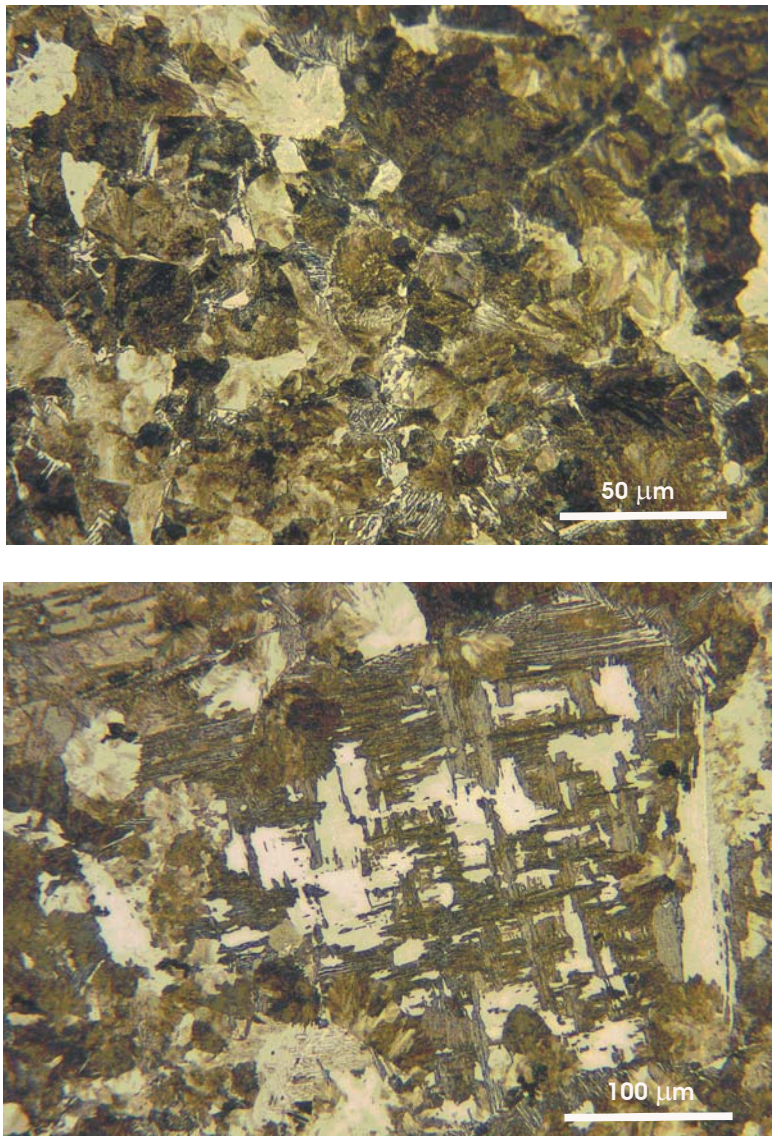

Figure 8: Post weld metallographic characterization of the weld HAZ showing pearlite formation (top) in the fine grain region of the HAZ, and bainite formation in the coarse grain region of the HAZ just adjacent to the fusion line.

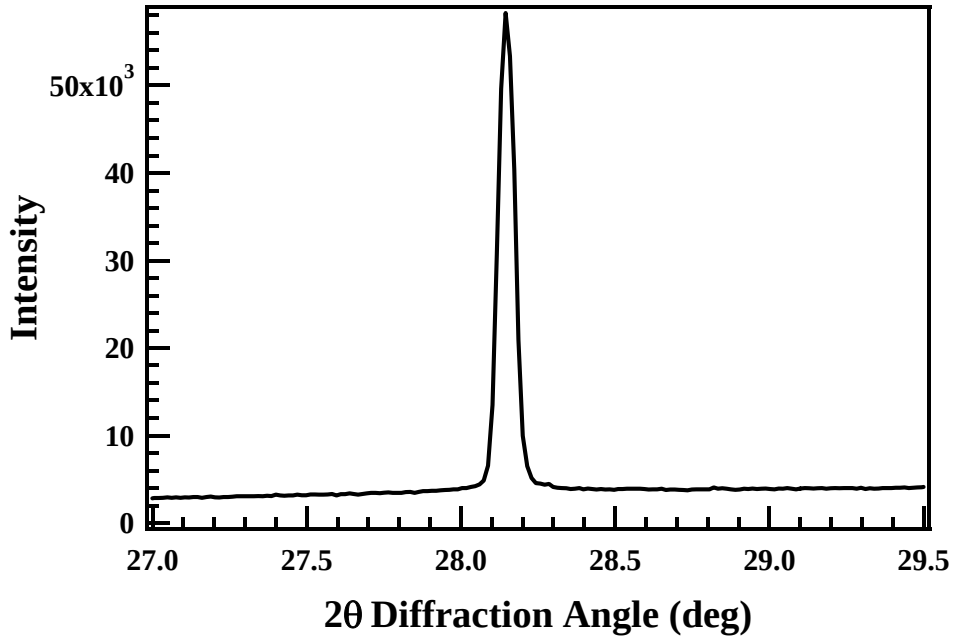

(a)

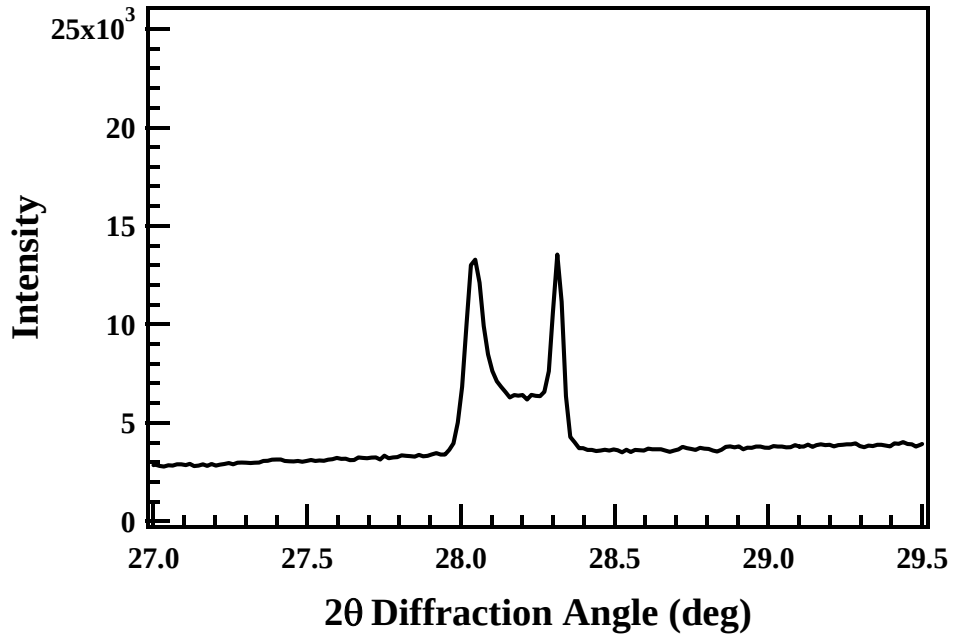

(b)

Figure 9: X-ray diffraction patterns taken at the X=0 mm location showing (a) splitting of the fcc(111) peak at Y=5.8 mm and (b) an fcc(111) peak located at Y=5.0 mm.

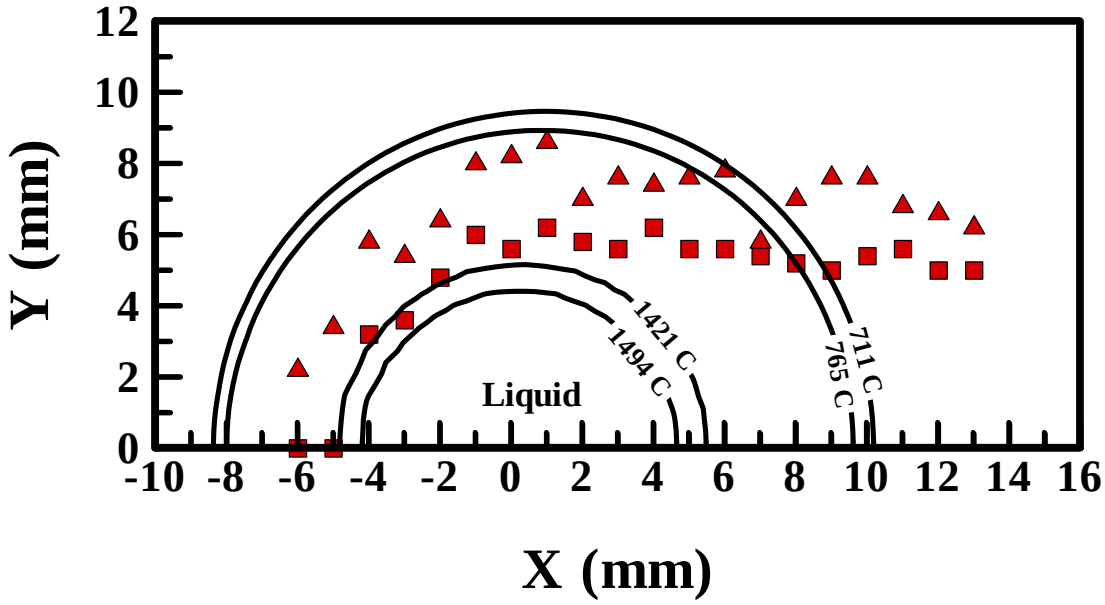

Figure 10: Weld map showing peak split regions compared to A1 and A3 isotherms. The triangles represent the location where splitting was first observed during heating, while the squares represent the location where the split peaks combine to form a single peak.

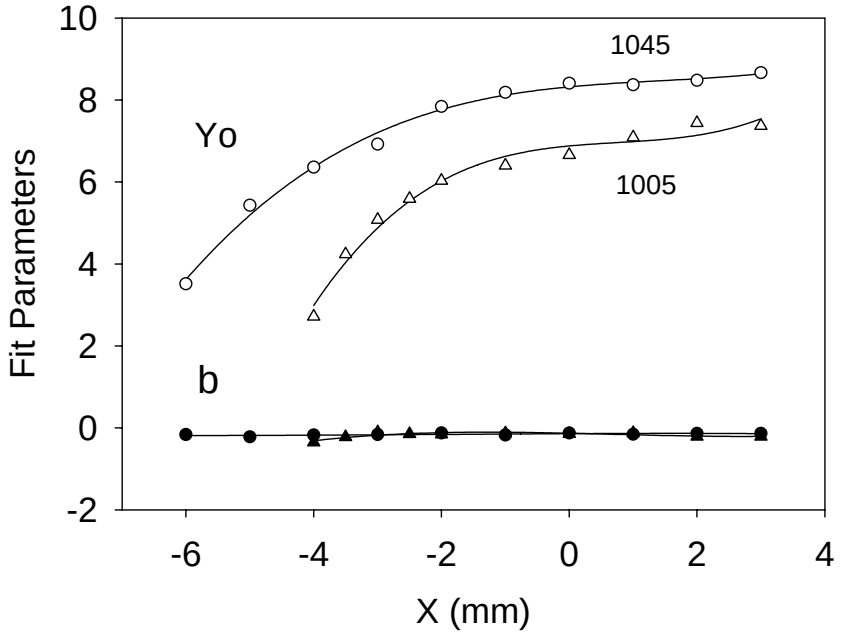

Figure 11: Sigmoidal fit parameters for the $\alpha \rightarrow \gamma$ transformation from the SRXRD data at different x-axis locations along the weld. The parameter y_o (open symbols) represents the location where 50% of the $\alpha \rightarrow \gamma$ transformation had taken place, and the b parameter (solid symbols) represents the rate of transformation. Data for both the 1045 steel (circles) and 1005 steel (triangles) are compared.